FABAD J. Pharm. Sci., 51, 3, 1227-1248, 2026
Doi: 10.55262/fabadeczacilik.1974032
RESEARCH ARTICLE

Multi-Scale *In Silico* Discovery of Potent SARS-CoV-2 RdRp Inhibitors

Sena ÇİNKILIÇ*, Erol AKGÜN**, Sevil ŞENKARDEŞ***, Necla KULABAŞ****°

Multi-Scale In Silico Discovery of Potent SARS-CoV-2 RdRp Inhibitors

SUMMARY

*In this study, fourteen 1,3-thiazolidin-4-one–benzenesulfonohydrazide derivatives were evaluated as potential SARS-CoV-2 RNA-dependent RNA polymerase (RdRp) inhibitor candidates using an integrated in silico approach. Molecular docking was performed using the 7BV2 RdRp-RNA complex. The predicted binding energies of the E and Z isomers of compounds **1-14** ranged from -8.01 to -9.27 kcal.mol^{-1}, corresponding to score-derived Ki estimates of 0.16-1.34 μM. For remdesivir monophosphate (RMP), the corresponding values were -9.72 kcal.mol^{-1} and 0.08 μM, respectively. Among the designed isomers, the Z isomer of compound **7** exhibited the most favorable binding profile (-9.27 kcal.mol^{-1}; estimated Ki = 0.16 μM). During 100 ns molecular dynamics simulations, the Z isomer maintained stable ligand RMSD values of approximately 1.1-1.5 Å, whereas the E isomer underwent an early conformational reorientation before stabilizing at approximately 3.3-3.7 Å. The Z isomer exhibited persistent interactions with Gly590, Thr591, Lys593, and Phe594. MM/GBSA analysis yielded average binding energies of -33.19 ± 2.97 and -24.29 ± 2.96 kcal.mol^{-1} for the Z and E isomers, respectively. DFT and condensed Fukui function analyses revealed isomer-dependent electronic reactivity, while SwissADME predicted low lipophilicity, high polarity, no Lipinski rule violations, and no cytochrome P450 inhibition for compound **7**. Overall, these findings support the Z isomer of compound **7** as a prioritized candidate for further optimization and experimental validation.*

Keywords: *SARS-CoV-2 RdRp, 1,3-thiazolidin-4-one, sulfonohydrazide, docking, DFT.*

Güçlü SARS-CoV-2 RdRp İnhibitörlerinin Çok Ölçekli İn Silico Yöntemlerle Keşfi

ÖZ

*Bu çalışmada, on dört 1,3-tiyazolidin-4-on-benzensülfonohidrazid türevi, bütünleşik bir in silico yaklaşım kullanılarak SARS-CoV-2 RNA-bağımlı RNA polimerazı (RdRp) için potansiyel inhibitör adayları olarak değerlendirilmiştir. Moleküler kenetleme, 7BV2 RdRp-RNA kompleksi üzerinden gerçekleştirilmiş ve Bileşik **1-14**'ün E ve Z izomerleri için öngörülen bağlanma enerjileri -8,01 ile -9,27 kcal.mol^{-1} arasında değişmiş ve skordan türetilen Ki tahminleri 0,16-1,34 μM olarak hesaplanmıştır. Remdesivir monofosfat (RMP) için bağlanma enerjisi ve Ki tahmini sırasıyla -9,72 kcal.mol^{-1} ve 0,08 μM'dir. Tasarlanan izomerler arasında bileşik 7'nin Z izomeri en elverişli bağlanma profilini göstermiştir (-9,27 kcal.mol^{-1}; tahmini Ki = 0,16 μM). Yüz nanosaniyelik moleküler dinamik simülasyonlarında Z izomeri yaklaşık 1,1-1,5 Å düzeyinde kararlı ligand RMSD değerlerini korurken, E izomeri erken dönemde konformasyonel yeniden yönlenme gösterdikten sonra yaklaşık 3,3-3,7 Å düzeyinde kararlı hale gelmiştir. Z izomeri Gly590, Thr591, Lys593 ve Phe594 ile kalıcı etkileşimler oluşturmuştur. MM/GBSA analizinde ortalama bağlanma enerjileri Z ve E izomerleri için sırasıyla -33,19 ± 2,97 ve -24,29 ± 2,96 kcal.mol^{-1} olarak bulunmuştur. DFT ve yoğunlaştırılmış Fukui analizleri izomere bağlı elektronik reaktiviteyi ortaya koyarken, SwissADME bileşik **7** için düşük lipofilisite, yüksek polarite, Lipinski kuralı ihlali bulunmaması ve sitokrom P450 inhibisyonu öngörülmemesi gibi özellikler göstermiştir. Bulgular, özellikle bileşik **7**'nin Z izomerini ileri optimizasyon ve deneysel doğrulama için öncelikli bir aday olarak desteklemektedir.*

Anahtar Kelimeler: *SARS-CoV-2 RdRp, 1,3-tiyazolidin-4-on, sülfonohidrazid, moleküler kenetleme, DFT.*

Recieved: 24.06.2026
Revised: 15.08.2026
Accepted: 19.08.2026

* ORCID: 0009-0008-2453-9672, Institute of Health Sciences, Marmara University, Istanbul, Türkiye
** ORCID: 0000-0001-7391-6157, Department of Pharmaceutical Chemistry, Faculty of Pharmacy, Marmara University, Istanbul, Türkiye
*** ORCID: 0000-0002-0523-459X, Department of Pharmaceutical Chemistry, Faculty of Pharmacy, Marmara University, Istanbul, Türkiye
**** ORCID: 0000-0003-2273-5094, Department of Pharmaceutical Chemistry, Faculty of Pharmacy, Marmara University, Istanbul, Türkiye

° Corresponding Author; Necla Kulabaş
E-mail: necla.kulabas@marmara.edu.tr

INTRODUCTION

Coronavirus disease 2019 (COVID-19), caused by severe acute respiratory syndrome coronavirus 2 (SARS-CoV-2), has posed an unprecedented global public health challenge since its emergence in late 2019 (Mammeri, Kerkour, Chafai, Harkat, & Chafaa, 2025). According to data reported by the World Health Organization (WHO), approximately 779 million confirmed cases have been documented worldwide since the onset of the pandemic (World Health Organization, n.d.). In response to this crisis, extensive research efforts have primarily focused on vaccine development to control viral transmission and mitigate disease severity. These vaccines are designed to elicit neutralizing antibodies against the viral spike (S) protein, thereby preventing viral entry into host cells. However, accumulating evidence indicates that vaccine-induced immunity may wane over time and exhibit reduced effectiveness against emerging variants (Gajjar, Dhameliya, & Shah, 2021; Mehyar et al., 2025).

In addition to vaccination strategies, antiviral agents have played a crucial role in the therapeutic management of COVID-19. Most antiviral drugs target key enzymes involved in viral replication, particularly RNA-dependent RNA polymerase (RdRp) and the 3C-like protease (main protease), which are essential for viral genome replication and protein processing (Wang, Anirudhan, Du, Cui, & Rong, 2021; Mehyar et al., 2025). Nevertheless, the continuous emergence of mutations in the SARS-CoV-2 genome, especially within genes encoding these target proteins, may lead to structural alterations that compromise the efficacy of existing therapeutics. This highlights the urgent need for the development of novel antiviral agents with improved selectivity and resistance profiles.

The infection mechanism of SARS-CoV-2 is initiated by the binding of the viral spike protein to the human angiotensin-converting enzyme 2 (ACE2) receptor, facilitating viral entry into host cells. Following entry, the virus exploits the host cellular machinery to translate viral polyproteins, which are subsequently cleaved into functional proteins. Central to the viral replication cycle is RdRp, which catalyzes the synthesis of a complementary negative-strand RNA using the positive-sense viral RNA genome as a template. This intermediate then serves as a template for the production of new viral RNA genomes. The replication process is mediated by the replication–transcription complex, in which the catalytic subunit nsp12 functions in conjunction with cofactors nsp7 and nsp8. RdRp is widely recognized as an attractive antiviral target because of its highly conserved active site and the lack of a homologous counterpart in human cells. Furthermore, this enzyme is conserved across a wide range of RNA viruses, including influenza virus and hepatitis C virus (HCV), making it a strategic target for the development of broad-spectrum antiviral agents (Gajjar et al., 2021; Wang et al., 2021).

Thiazolidin-4-one represents an important heterocyclic scaffold with well-documented biological activities. Compounds bearing this core structure have been reported to exhibit a broad spectrum of pharmacological effects, including antibacterial (Kline et al., 2009; Şenkardeş, Kart, Bebek, Gündüz, & Küçükgüzel, 2023), anticancer (Şenkardeş & Küçükgüzel, 2016; Thakkar, Vaghani, Kardani, & Patel, 2025) and antiviral activities (Cihan-Üstündağ, Gürsoy, Naesens, Ulusoy-Güzeldemirci, & Çapan, 2016). Notably, 1,3-thiazolidin-4-one derivatives have been shown to inhibit HCV NS5B RdRp (Kulabaş, Lee, Bingöl Özakpınar, & Küçükgüzel, 2024). The reported structural and functional similarities between HCV NS5B RdRp polymerase and SARS-CoV-2 RdRp suggest that such compounds may also act as potential inhibitors of SARS-CoV-2 replication machinery (Elghoneimy, Ismail, Boeckler, Azzazy, & Ibrahim, 2021). Moreover, the incorporation of additional pharmacophoric moieties, such as benzene sulfonohydrazide groups, into the molecular framework may enhance binding affinity through the formation of additional hydrogen

bonding interactions between sulfonyl oxygen atoms and hydrazide NH groups with amino acid residues in the active site of the target enzyme (El-Hddad, Sobhy, El-morsy, Shoman, & El-Adl, 2024). Such rational structural modifications represent an effective strategy in the design of potent and selective enzyme inhibitors.

Taken together, these findings indicate that hybrid molecules integrating the 1,3-thiazolidin-4-one scaffold with benzene sulfonohydrazide moieties may serve as promising candidates for targeting SARS-CoV-2 RdRp. In this context, the present study aims to comprehensively evaluate the inhibitory potential of these compounds against SARS-CoV-2 RdRp using *in silico* approaches. This study is expected to contribute to the rational design and development of novel antiviral agents targeting SARS-CoV-2.

MATERIALS AND METHODS

Molecular docking analysis

Three-dimensional conformations of the novel 1,3-thiazolidin-4-one derivatives, investigated as potential SARS-CoV-2 RdRp inhibitors, were generated using the semi-empirical PM3 method implemented in Spartan 04 (SPARTAN 04, Wavefunction, Inc., Irvine, CA, USA) (Wavefunction Inc., 2004). For each compound, two geometrical isomers corresponding to the *E* and *Z* configurations were constructed and subjected to full geometry optimization at the PM3 level of theory. The optimized structures were saved in PDB format for subsequent molecular docking studies. The prepared three-dimensional ligand structures were then processed using AutoDockTools (ADT, version 1.5.7) (Morris et al., 2009). Polar hydrogen atoms were added, Gasteiger partial atomic charges were assigned, and rotatable bonds were defined. Finally, all ligands were converted into PDBQT format for docking simulations.

The cryo-electron microscopy structure of the SARS-CoV-2 RNA-dependent RNA polymerase (RdRp) complex bound to template–primer RNA and remdesivir was retrieved from the Protein Data Bank (PDB ID: 7BV2) (Yin et al., 2020). The structure was determined at a resolution of 2.50 Å and comprises the catalytic nsp12 subunit together with the accessory proteins nsp7 and nsp8, as well as template and primer RNA strands. In the experimental structure, remdesivir is covalently incorporated into the primer RNA strand and is present as remdesivir monophosphate (RMP). The pyrophosphate molecule and solvent molecules were removed, whereas the template-primer RNA strands and structurally relevant metal ions were retained to preserve the catalytic environment of the RdRp complex. For docking validation, the covalent bond connecting RMP to the primer RNA strand was removed, and the affected atoms were adjusted to ensure chemically appropriate valence and charge states. RMP was subsequently extracted and used as the reference ligand for redocking. The remaining RdRp-RNA complex was prepared using AutoDockTools. Polar hydrogen atoms were added, Gasteiger-Marsili partial atomic charges were assigned, and the prepared receptor was converted to PDBQT format. The docking grid was centered on the experimentally resolved position of RMP in the 7BV2 structure. The grid center coordinates were set to x = 91.537, y = 92.474, and z = 103.801 Å, with box dimensions of 24 × 24 × 24 Å. An exhaustiveness value of 64 was used for all docking calculations. The docking protocol was validated by redocking RMP into the experimentally defined RMP region using AutoDock Vina (v.1.2.7) (Trott & Olson, 2010; Eberhardt, Santos-Martins, Tillack, & Forli, 2021). The redocked pose was compared with the experimentally resolved RMP geometry after structural alignment. The heavy-atom root mean square deviation (RMSD) between the experimental and redocked poses was 1.097 Å, indicating successful reproduction of the experimentally resolved RMP orientation.

Following successful redocking validation, the experimentally defined RMP-binding region was selected as the standardized docking search space. The *E* and *Z* isomers of compounds **1**-**14** were subsequently docked into the same RMP-centered search space

using identical docking parameters. The receptor was treated as rigid, whereas ligand flexibility was allowed through predefined rotatable bonds. Multiple binding poses were generated for each ligand, and the pose with the most favorable AutoDock Vina score was selected for subsequent analysis.

The AutoDock Vina binding affinity scores were additionally converted into estimated dissociation constants (K_i) using the relationship $K_i = e^{\Delta G/RT}$ where R is the gas constant (0.0019872 kcal.mol^{-1}.K^{-1}) and T is the absolute temperature (298.15 K). The calculated K_i values were expressed in micromolar units. Protein–ligand interactions were examined using Discovery Studio Visualizer (BIOVIA, 2025), focusing on hydrogen bonding, hydrophobic interactions, π-π stacking, and electrostatic contacts within the catalytic region.

Molecular dynamics simulation analysis

Based on the selected docking pose, the protein–RNA–ligand complex was prepared for molecular dynamics (MD) simulations using AMBER 26 and AmberTools 26 (Götz et al., 2012; Salomon-Ferrer, Götz, Poole, Le Grand, & Walker, 2013; Case et al., 2023, 2025). The system contained the protein, two RNA chains, two structural Zn^{2+} ions, two Mg^{2+} ions, and the ligand. Protein and RNA were described using the ff14SB and OL3 force fields, respectively. The ligand was parameterized using GAFF2 with AM1-BCC partial atomic charges generated by Antechamber, and missing parameters were assigned using parmchk2. The two structural Zn^{2+} sites were treated using the ZAFF bonded model. The first Zn^{2+} ion was coordinated by His295, Cys301, Cys306, and Cys310, whereas the second was coordinated by His642, Cys487, Cys645, and Cys646. Coordinating histidines and cysteines were assigned the corresponding ZAFF residue types, and explicit Zn–N and Zn–S bonds were included during topology generation. The two Mg^{2+} ions were retained as nonbonded divalent ions using standard TIP3P-compatible 12-6 parameters without explicit Mg–ligand bonds.

The complex was solvated in an explicit TIP3P water box with a 10 Å solvent buffer, and Na^+ counterions were added to neutralize the system. Energy minimization was performed in successive stages with progressively reduced positional restraints on non-hydrogen solute atoms, starting at 10 kcal.mol^{-1} Å^{-2}, followed by 5 kcal.mol^{-1} Å^{-2} and subsequently weaker restraints before a final unrestrained minimization. The 5′-terminal G5 and U5 residues were additionally restrained during the restrained minimization stages.

The minimized system was gradually heated from 10 to 300 K under the NVT ensemble using a Langevin thermostat and a 1 fs integration time step while maintaining positional restraints on the solute. This was followed by 500 ps of NVT equilibration at 300 K using a 2 fs time step, SHAKE constraints on bonds involving hydrogen atoms, a Langevin collision frequency of 2 ps^{-1}, and positional restraints of 5 kcal.mol^{-1} Å^{-2} on non-hydrogen solute atoms.

Pressure equilibration was subsequently performed under the NPT ensemble in three stages at 300 K and 1 bar. The system was equilibrated for 500 ps with restraints of 5 kcal.mol^{-1} Å^{-2}, followed by 500 ps with restraints reduced to 1 kcal.mol^{-1} Å^{-2}, and finally for 1 ns without restraints. A 2 fs integration time step and SHAKE constraints were applied throughout the NPT equilibration, resulting in a total NPT equilibration period of 2 ns.

Following equilibration, an unrestrained 100 ns conventional MD simulation was performed under NPT conditions at 300 K and 1 bar using a 2 fs integration time step. Temperature was controlled using a Langevin thermostat with a collision frequency of 2 ps^{-1}, and the pressure relaxation time was set to 2 ps. A nonbonded cutoff of 10 Å was applied, periodic boundary conditions were used, and bonds involving hydrogen atoms were constrained using SHAKE.

Trajectory analyses were performed using cpptraj in AmberTools 26. Protein structural stability and flexibility were assessed using backbone RMSD and

residue-wise RMSF, while overall structural compactness was evaluated using the radius of gyration (Rg). RNA stability was assessed using heavy-atom RMSD and, where appropriate, residue-wise RMSF. Ligand heavy-atom RMSD was calculated after alignment to the receptor to monitor retention of the binding pose throughout the simulation.

Protein–ligand and RNA-ligand interactions were characterized using ProLIF (v2.2.1) (Bouysset & Fiorucci, 2021; Bouysset, 2026) by evaluating the occurrence and occupancy of hydrogen-bonding, hydrophobic, ionic, π-π, cation-π, and van der Waals interactions. Metal coordination was analyzed separately using distance- and angle-based trajectory analyses.

Relative receptor–ligand binding energetics were estimated using the MM/GBSA approach implemented in MMPBSA.py within AmberTools 26. Explicit water molecules and freely diffusing counterions were removed before the calculations. The receptor was defined as the protein, RNA chains, and retained structural Zn^{2+} and Mg^{2+} ions, whereas the small molecule was defined as the ligand.

Density functional theory analysis

Density Functional Theory (DFT) calculations for the *E* and *Z* isomers of compound **7** were performed using Gaussian 16 (Frisch et al., 2016), and molecular visualizations were generated with GaussView 6 (Dennington, Keith, & Millam, 2016). Geometry optimizations and frequency calculations were carried out at the B3LYP/6-31G(d) level using the options Opt=(CalcFC, MaxStep=5), Int=UltraFine, and SCF=Tight. Solvent effects were modeled with the SMD implicit solvation model *via* SCRF=(SMD, Solvent=Water). The optimized geometries were confirmed to correspond to true minima by the absence of imaginary frequencies. In addition, HOMO and LUMO energies (including the HOMO-LUMO gap) were obtained, and cube files were generated for electrostatic potential (ESP) and electron density analyses. Single-point (SP) DFT calculations were performed on the optimized geometries at the B3LYP/6-31G(d) level using Int=UltraFine and SCF=(XQC,Tight). Solvent effects were modeled with the SMD implicit solvation model in water (SCRF=(SMD, Solvent=Water)). The wavefunction and geometry were read from the checkpoint file of the preceding optimization (Geom=AllCheck, Guess=Read), and atomic charges were obtained *via* NBO/NPA analysis (Pop=(NBORead)). In addition, based on the optimized neutral geometry, single-point DFT calculations were carried out for the neutral (N), anion (N+1), and cation (N−1) species at the ωB97X-D/def2-SVP level (Int=UltraFine, SCF=Tight, SMD/water). Atomic charges were computed using Hirshfeld population analysis (Pop=Hirshfeld), and condensed Fukui functions were derived from these charges as follows:

$$f_k^+ = q_k(N) - q_k(N+1) \quad (1)$$

$$f_k^- = q_k(N-1) - q_k(N) \quad (2)$$

$$f_k^0 = \frac{q_k(N-1) - q_k(N+1)}{2} \quad (3)$$

$$\Delta f = \frac{f_k^+ + f_k^-}{2} \quad (4)$$

In these expressions, q_k represents the Hirshfeld atomic charge on atom k, and *N*, *N*+1 and *N*-1 correspond to the neutral, anion, and cationic states, respectively. Thus, f_k^+, f_k^-, and f_k^0 refer to the condensed Fukui functions for nucleophilic, electrophilic, and radical attack, respectively.

***In silico* ADME profiling and metabolite prediction**

The pharmacokinetic properties and drug-likeness profiles of the designed compounds **1-14** were evaluated using the online tool SwissADME (http://www.swissadme.ch) (Daina, Michielin, & Zoete, 2017). The chemical structures of the compounds were drawn and converted into SMILES format prior to submission. SwissADME was employed to predict key physicochemical parameters, including molecular weight (MW), lipophilicity (LogP), topological polar surface area (TPSA), number of hydrogen bond donors and acceptors. Also, pharmacokinetic properties

such as gastrointestinal (GI) absorption, blood–brain barrier (BBB) permeability, and cytochrome P450 (CYP) enzyme inhibition profiles were evaluated. In addition, drug-likeness was assessed according to Lipinski's rule of five.

The metabolic fate of compound **7** with the best binding affinity was predicted using BioTransformer 3.0 (Djoumbou Feunang et al., 2019; Wishart et al., 2022). The SMILES representations of the compounds were used as input for the prediction of biotransformation pathways. BioTransformer 3.0 integrates both knowledge-based and machine learning approaches to simulate Phase I and Phase II metabolic reactions. Cytochrome P450-mediated transformations, including oxidation, reduction, and hydrolysis reactions, were analyzed under the "Human Cytochrome P450 (CYP450)" module. Additionally, conjugation reactions such as glucuronidation and sulfation were predicted using the Phase II metabolism module.

RESULTS AND DISCUSSION

Molecular docking analysis

The docking protocol was first validated by redocking remdesivir monophosphate (RMP) into the experimentally defined binding region of the SARS-CoV-2 RdRp-RNA complex (PDB ID: 7BV2). Superimposition of the redocked RMP pose with its experimentally resolved conformation yielded a heavy-atom root mean square deviation (RMSD) of 1.097 Å , which is below the commonly accepted 2.0 Å threshold for successful redocking validation (Figure 1.). The close agreement between the two conformations demonstrated that the selected docking protocol and grid definition could reproduce the experimentally resolved orientation of RMP within the RdRp catalytic region.

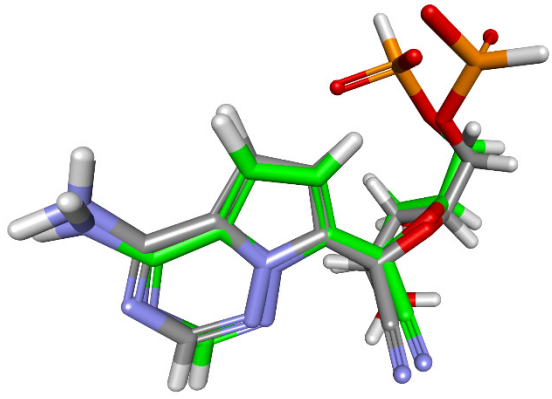

Figure 1. Superimposition of the experimentally resolved (7BV2) and redocked poses of remdesivir monophosphate (RMP) within the SARS-CoV-2 RdRp-RNA catalytic region

Using the validated protocol, the *E* and *Z* isomers of compounds **1-14** were docked using RMP as the reference ligand. Predicted binding energies ranged from -8.01 to -9.27 kcal.mol^{-1}, corresponding to score-derived K_i estimates of 0.16-1.34 μM (Table 1.). RMP showed a binding energy of -9.72 kcal.mol^{-1} and an estimated K_i of 0.08 μM. Among the designed compounds, the *Z* isomer of compound **7** showed the most favorable binding profile (-9.27 kcal.mol^{-1}; estimated K_i = 0.16 μM), while its *E* isomer also exhibited favorable binding (-8.78 kcal.mol^{-1}; estimated K_i = 0.37 μM). Accordingly, compound **7** was selected for further *in silico* analyses.

Table 1. Binding energy (kcal.mol^{-1}) and estimated dissociation constants (K_i) of the *E* and *Z* isomers of compounds **1-14** and RMP against SARS-CoV-2 RdRp

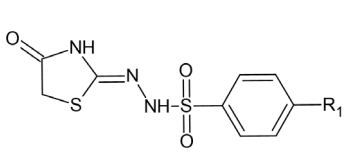
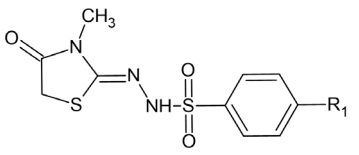

Compound	R_1	*E* isomer		*Z* isomer	
		Binding Energy	Estimated K_i (μM)	Binding Energy	Estimated K_i (μM)
1	-H	-8.48	0.61	-8.72	0.41
2	-CH_3	-8.72	0.41	-9.18	0.19
3	-F	-8.77	0.37	-9.09	0.22
4	Cl	-8.55	0.54	-9.02	0.24
5	Br	-8.27	0.87	-9.04	0.24
6	-OCH_3	-8.85	0.33	-9.01	0.25
7	-NO_2	-8.78	0.37	-9.27	0.16
8	-H	-8.01	1.34	-8.45	0.64
9	-CH_3	-8.43	0.66	-8.83	0.34
10	-F	-8.40	0.70	-8.81	0.35
11	Cl	-8.36	0.74	-8.69	0.43
12	Br	-8.13	1.10	-8.32	0.80
13	-OCH_3	-8.44	0.65	-8.30	0.82
14	-NO_2	-8.33	0.78	-8.71	0.41
RMP		-9.72 kcal.mol^{-1}	Estimated K_i = 0.08 μM		

Estimated K_i values were derived from AutoDock Vina binding affinity scores using $K_i = e^{\Delta G/RT}$ at 298.15 K.

RMP exhibited a diverse interaction network within the RdRp binding site, including hydrogen bonds with U10 (chain T), U20 (chain P), and Ser759, π–π interactions with A11 (chain T) and U20 (chain P), and a π–cation interaction involving Arg555 (Figure 2.). Both the *E* and *Z* isomers of compound **7** formed hydrogen bonds with Lys593 and Gly590. The sulfonyl group contributed to hydrogen bonding with Lys593, while the 1,3-thiazolidin-4-one moiety participated in the interaction with Gly590. In addition, the aromatic portion of compound **7** was involved in π-cation interactions with Lys593, whereas the nitro-substituted region showed additional electrostatic contacts involving Asp865. Notably, the *Z* isomer established an additional hydrogen bond with the RNA nucleotide A19 (chain P) through the N-H functionality of the 1,3-thiazolidin-4-one ring. The presence of this additional RNA-mediated interaction, together with the interactions shared by both isomers, may contribute to the more favorable predicted binding affinity of the *Z* isomer.

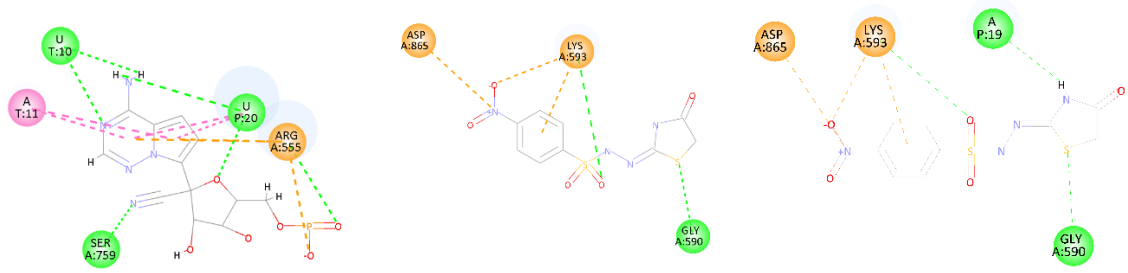

RMP **Compound 7_*E* isomer** **Compound 7_*Z* isomer**

Figure 2. Binding poses of remdesivir and compound **7** with 2D diagrams

Molecular dynamics simulation analysis

The ligand RMSD profiles obtained from the molecular dynamics simulations revealed distinct conformational behaviors for the *E* and *Z* isomers of compound **7** (Figure 3.). The *Z* isomer rapidly reached equilibrium during the initial stage of the simulation and subsequently maintained relatively low RMSD values, predominantly within the range of approximately 1.1-1.5 Å throughout the 100 ns simulation, indicating a stable bound conformation. In contrast, the *E* isomer exhibited greater conformational rearrangement during the early stage of the simulation. After initial fluctuations, its RMSD increased markedly at approximately 10 ns and stabilized at a higher plateau of approximately 3.3-3.7 Å for the remainder of the simulation. This behavior suggests that the *E* isomer underwent a substantial conformational reorientation relative to its initial docking pose before reaching a new stable conformational state. Overall, the lower and more consistent RMSD values observed for the *Z* isomer indicate greater conformational stability relative to the *E* isomer.

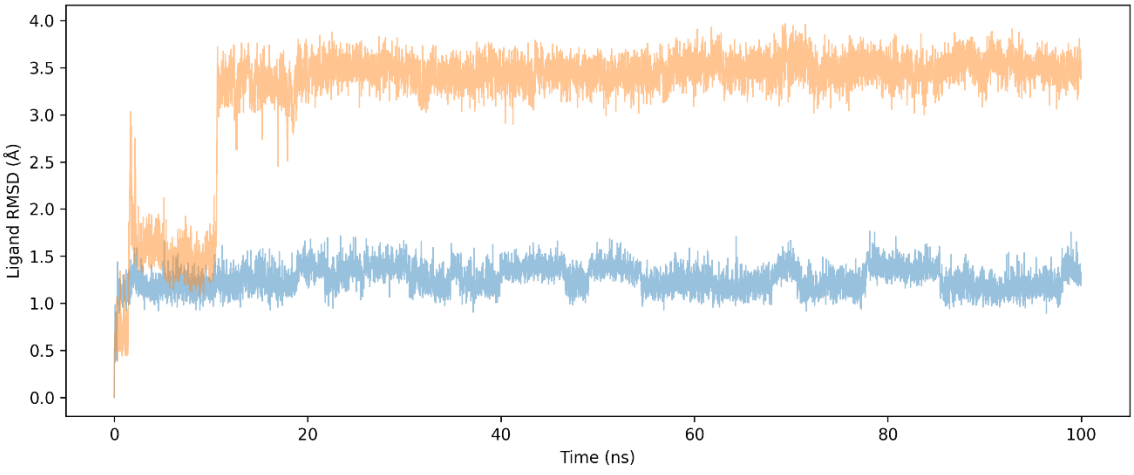

Figure 3. The RMSD profile of the *Z* isomer of compound **7** is shown in blue, while the RMSD profile of the *E* isomer is shown in orange

The RMSF profiles of chain A (residues 84-929) were generally similar for the *E*- and *Z*-isomer-bound complexes, with most residues exhibiting low fluctuations (Figure 4.). Although localized differences were observed, the *E* isomer-bound complex showed higher RMSF values in several regions, particularly toward the C-terminal part of the protein. These findings suggest that both isomers maintain a broadly comparable protein flexibility profile, while the *Z* isomer may provide slightly greater local stabilization in selected regions.

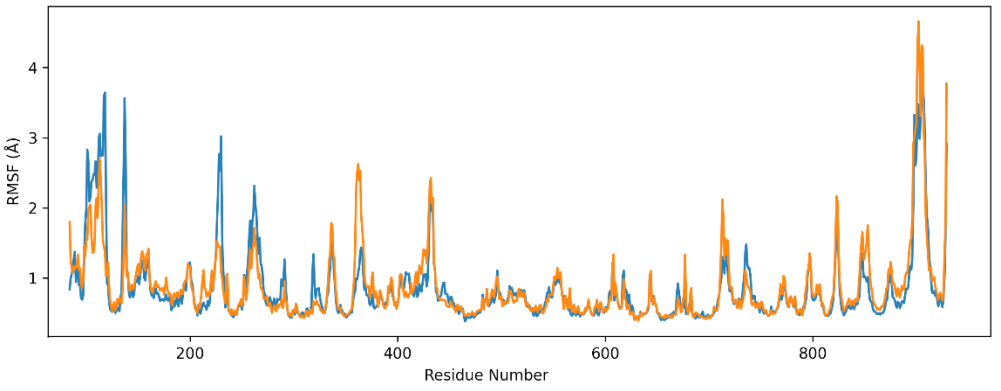

Figure 4. RMSF values of the chain A (84-929) bound to the *Z* isomer of compound **7** are shown in blue, whereas those of the chain A (84-929) bound to the *E* isomer of compound **7** are shown in orange

The buried surface area (BSA) profiles of the *E* and *Z* isomers of compound **7** exhibited considerable fluctuations throughout the 100 ns simulation (Figure 5.). Although the BSA values of the two complexes frequently overlapped, the *Z* isomer generally displayed higher BSA values than the *E* isomer, particularly during the middle and later stages of the simulation. This trend suggests a relatively larger and more persistent buried protein-ligand interface for the *Z* isomer. Nevertheless, transient decreases and frequent crossings between the two profiles indicate dynamic changes in the extent of protein-ligand contact during the simulation. Overall, the BSA analysis suggests that the *Z* isomer maintains a somewhat more extensive interaction interface with the protein than the *E* isomer.

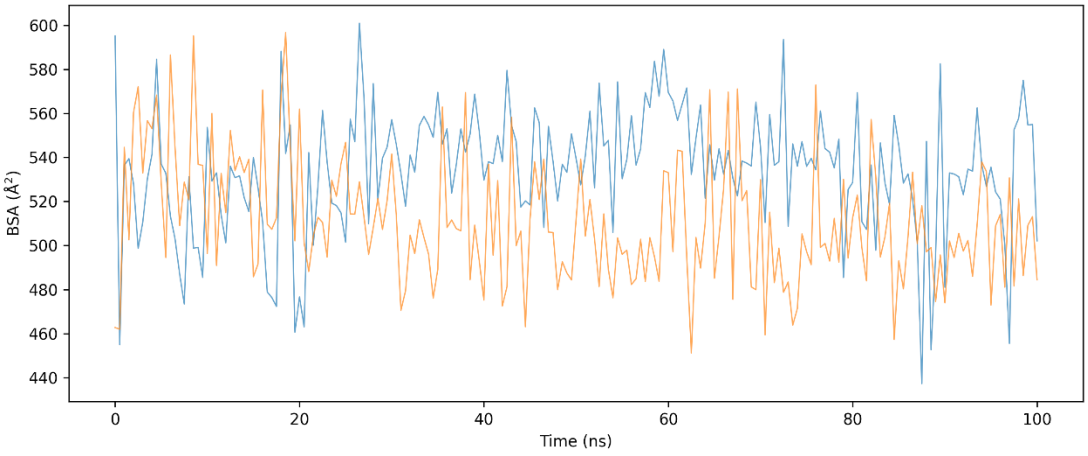

Figure 5. The BSA formed between the enzyme and the *Z* isomer of compound **7** is shown in blue, whereas the BSA formed between the enzyme and the *E* isomer of compound **7** is shown in orange

The interaction fingerprint analysis of the *Z* isomer of compound **7** revealed a highly persistent interaction network involving Gly590, Thr591, Lys593, and Phe594 throughout the 100 ns simulation (Figure 6.). Hydrogen-bond interactions involving Gly590 and Thr591 were maintained for 99.37% and 99.35% of the trajectory, respectively, while Lys593 participated in hydrogen-bonding interactions with an occurrence of 76.29%. In addition, highly persistent hydrophobic contacts were observed with Phe594 (99.82%) and Lys593 (99.78%). Lys593 also contributed through intermittent π-cation interactions (15.37%), highlighting its involvement through multiple interaction modes. Less frequent interactions included π-stacking

with U18 (8.34%) and hydrogen-bonding with A19 (4.59%). Overall, these findings indicate that the *Z* isomer is predominantly stabilized by persistent interactions within the Gly590–Phe594 region, with Lys593 appearing to play a particularly important role in maintaining the ligand–binding site interaction.

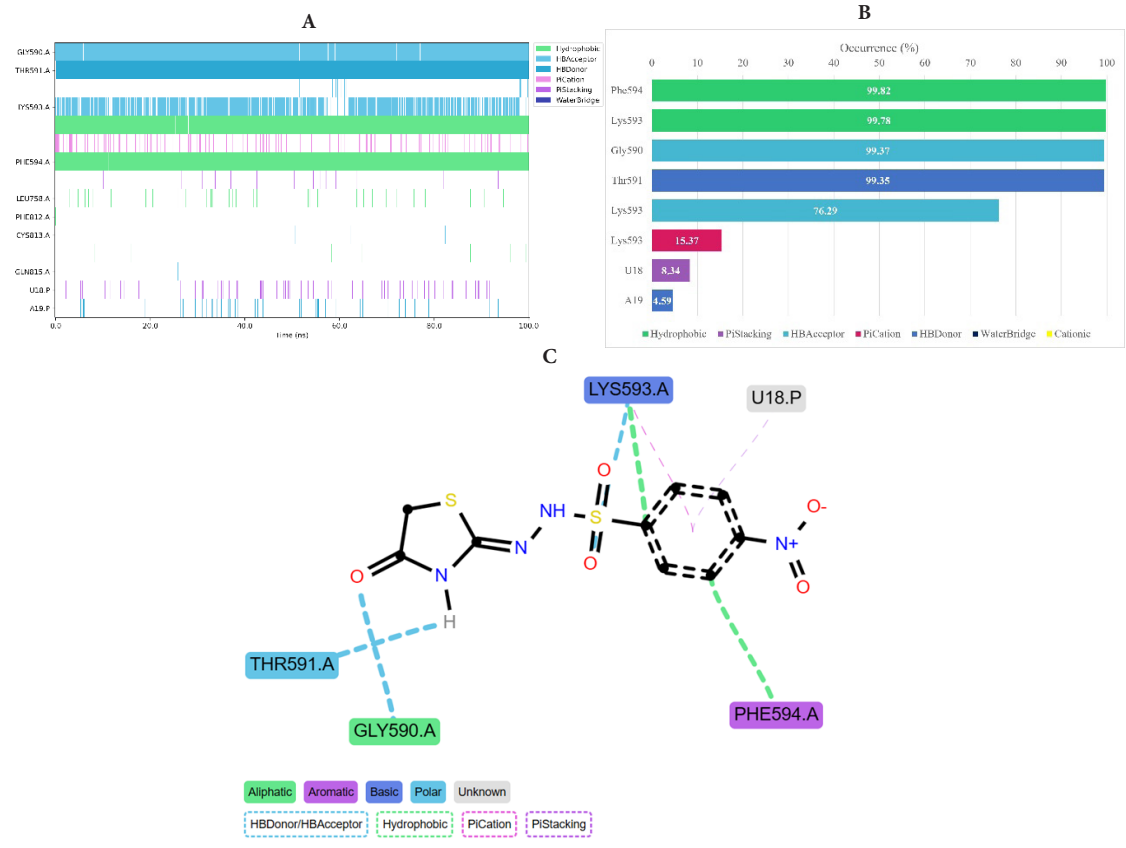

Figure 6. (A) Time-dependent interactions of the *Z* isomer of compound **7** with amino acid residues. (B) Percentage distribution of amino acid–interaction profiles for the *Z* isomer of compound **7**. (C) Two-dimensional (2D) representation of the interaction network of the *Z* isomer of compound **7**

The interaction fingerprint analysis of the *E* isomer of compound **7** revealed a persistent and diverse interaction network throughout the 100 ns molecular dynamics simulation (Figure 7.). The most prominent interactions were hydrophobic contacts with Lys593 (99.71%), Phe594 (97.11%), Trp598 (86.24%), and Met601 (82.18%), indicating the persistence of an extensive hydrophobic interaction network during most of the trajectory. In addition, a water-mediated interaction involving Gly590 was observed for 76.29% of the simulation. Lys593 also contributed through a π-cation interaction with an occurrence of 55.06% and an H-bond acceptor-type interaction with an occurrence of 25.36%, demonstrating the involvement of this residue through multiple interaction modes. Additional, less frequent interactions included a water bridge with A19 (31.37%), an H-bond acceptor-type interaction with U18 (22.99%), and a water-mediated interaction with A13 (12.97%). Overall, these results indicate that the stability of the *E* isomer within the binding site is predominantly supported by persistent hydrophobic interactions, complemented by water-mediated, hydrogen-bonding, and π-cation interactions.

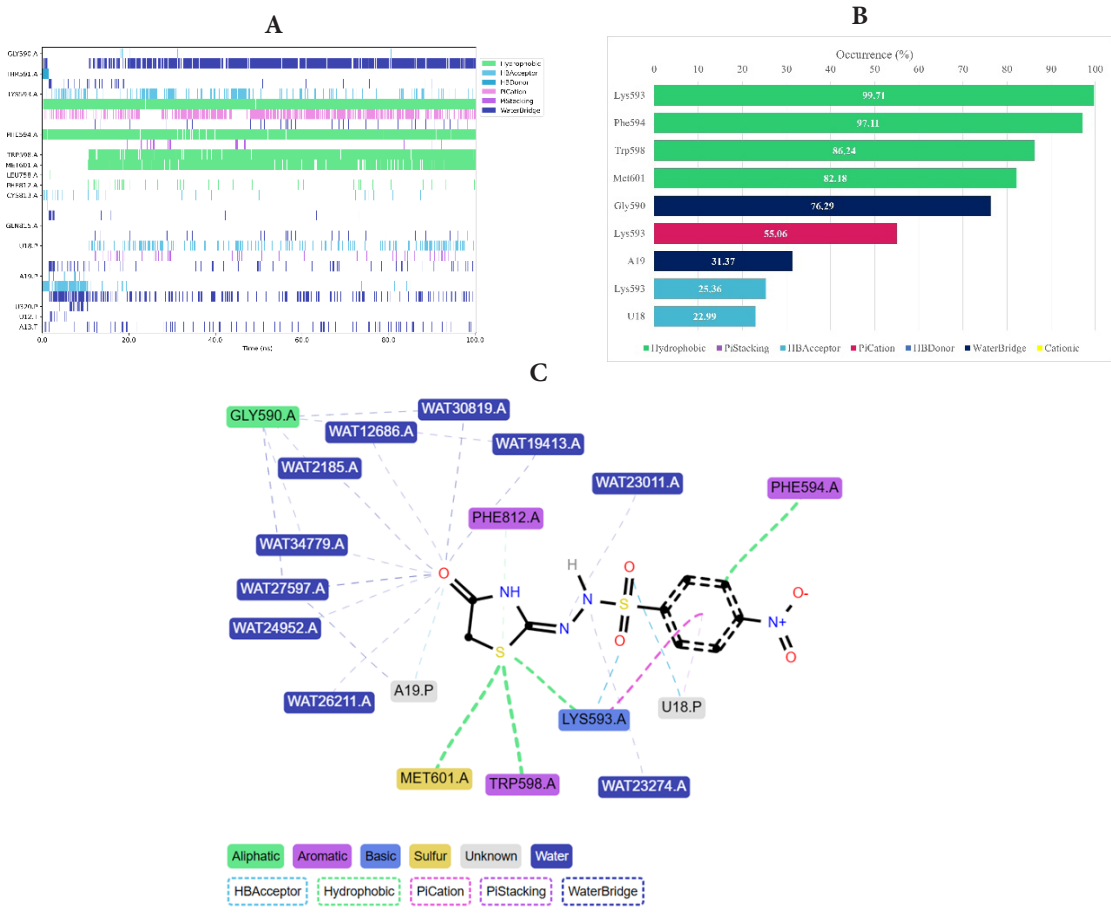

Figure 7. (A) Time-dependent interactions of the *E* isomer of compound **7** with amino acid residues. (B) Percentage distribution of amino acid–interaction profiles for the *E* isomer of compound **7**. (C) Two-dimensional (2D) representation of the interaction network of the *E* isomer of compound **7**

Time-dependent MM/GBSA analysis revealed that the *Z* isomer of compound **7** generally exhibited more favorable (more negative) binding energies than the *E* isomer throughout the 100 ns simulation (Figure 8.). Although transient fluctuations and occasional convergence of the energy profiles were observed, particularly around 80 ns, the *Z* isomer maintained consistently lower binding energies over most of the trajectory. The average MM/GBSA binding energy was -33.19 ± 2.97 kcal.mol^{-1} for the *Z* isomer and -24.29 ± 2.96 kcal.mol^{-1} for the *E* isomer. These results indicate a substantially more favorable predicted binding energetics for the *Z* isomer and further support its stronger interaction with the RdRp binding site compared with the *E* isomer.

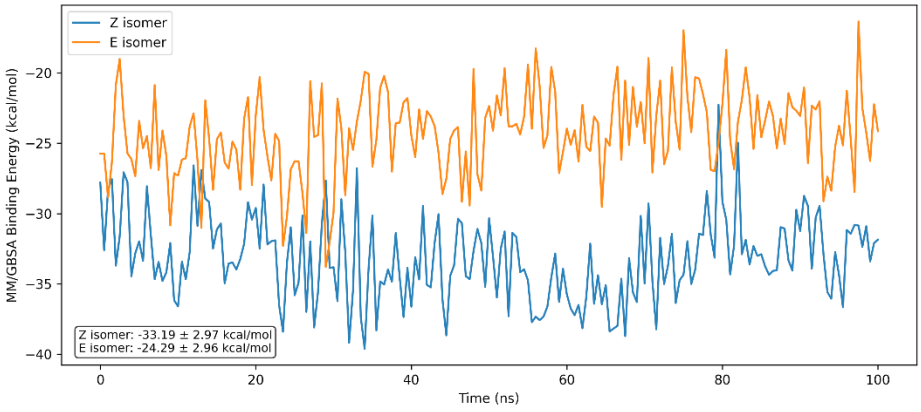

Figure 8. Time-dependent MM/GBSA binding energy profiles (ΔG) of the *Z* and *E* isomers of compound **7**. Calculations were performed using the Generalized Born (GB) model. The *Z* isomer is shown in blue and the *E* isomer in orange

DFT analysis

Based on analyses of the optimized geometries, including HOMO/LUMO energies, dipole moments, and electronic energies of the *E* and *Z* isomers of compound **7** (Table 2.), the *E* isomer was found to be slightly lower in energy than the *Z* isomer, while the *Z* isomer exhibits a higher dipole moment. In addition, the *Z* isomer shows a smaller HOMO-LUMO energy gap (E_{LUMO} - E_{HOMO}), suggesting that the *Z* isomer may be more readily excited than the *E* isomer.

Table 2. Some properties of optimized geometries of *E* and *Z* isomers of compound **7**

Compound	E_{HOMO} (kcal.mol^{-1})	E_{LUMO} (kcal.mol^{-1})	E_{LUMO}-E_{HOMO} (kcal. mol^{-1})	Dipole Moment (Debye)	Electronic Energy (Hartree)
***Z* isomer**	-153.859	-69.472	84.387	5.992	-1739.259
***E* isomer**	-160.542	-69.013	91.529	5.539	-1739.262

The optimized geometries of the *Z* and *E* isomers of compound **7** and their corresponding ESP surfaces are presented in Figure 9. The ESP distributions are qualitatively similar for both isomers. In both structures, the phenyl ring and the thiazolidin-4-one core appear relatively electron-deficient, whereas the sulfonyl and nitro groups, as well as the oxygen atoms in the thiazolidin-4-one moiety, exhibit electron-rich regions.

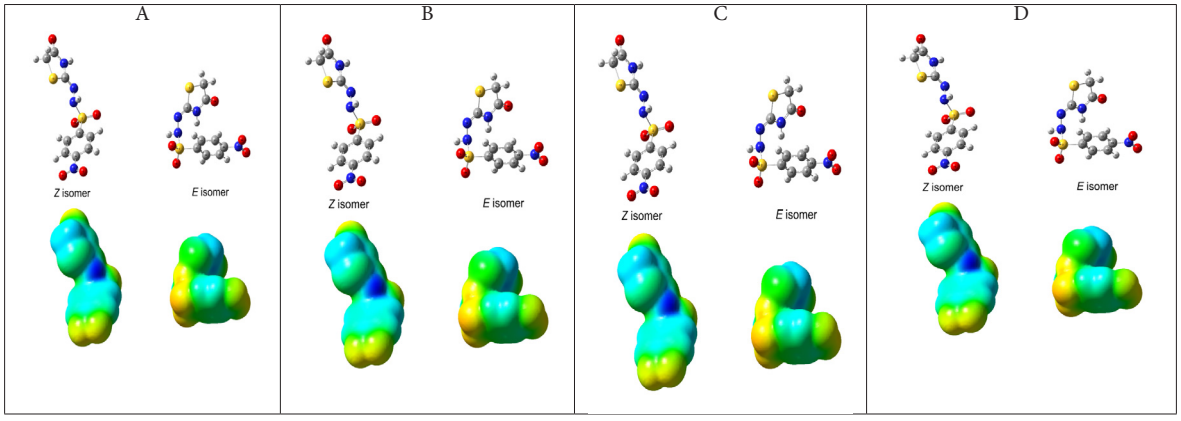

Figure 9. Optimized geometries of the *Z* (top left) and *E* (top right) isomers of compound **7**, and their corresponding electrostatic potential (ESP) surfaces (bottom left and bottom right, respectively)

In the HOMO–LUMO analysis of the optimized structures (Figure 10.), the HOMO is predominantly localized on the thiazolidin-4-one ring and the attached hydrazone unit, whereas the LUMO is mainly distributed over the nitrophenyl moiety, indicating a donor–acceptor character with charge-transfer propensity upon excitation.

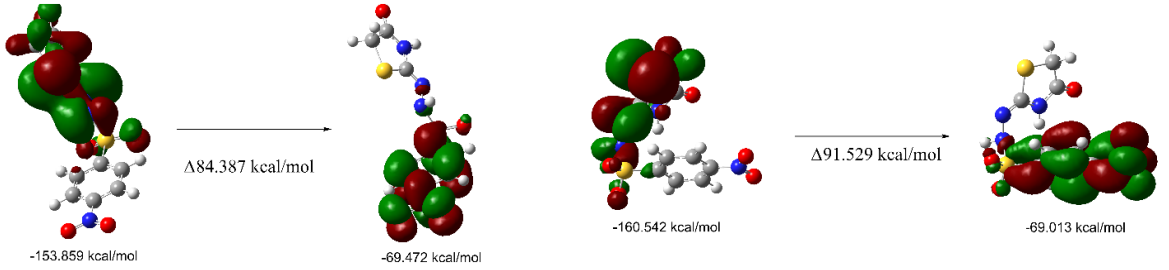

Figure 10. HOMO and LUMO distributions and the corresponding energy gaps of the *Z* (left) and *E* (right) isomers of compound **7**

The natural charge values obtained from the natural bond orbital (NBO) analysis of the isomers of compound **7** are presented in Table 3. The electron density at the S19 atom is higher in the *Z* isomer than in the *E* isomer. Similarly, the N10 and N11 atoms also exhibit higher electron density in the *Z* isomer. Overall, these findings indicate that the charge distribution is more uniform in the *Z* isomer, whereas, in the *E* isomer, the charge distribution is shifted more toward the sulfonohydrazide nitrogen atoms.

Table 3. Natural charge analysis of *Z* and *E* isomers of compound **7**

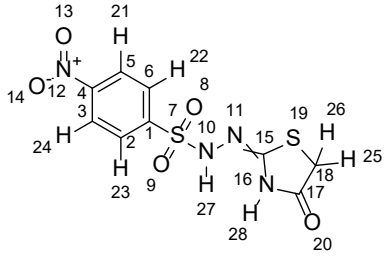

Atom No	Natural Charge of *Z* isomer	Natural Charge of *E* isomer	Atom No	Natural Charge of *Z* isomer	Natural Charge of *E* isomer
C1	-0.315	-0.312	**C15**	0.279	0.291
C2	-0.195	-0.201	**N16**	-0.635	-0.648
C3	-0.194	-0.194	**C17**	0.720	0.726
C4	0.078	0.076	**C18**	-0.685	-0.690
C5	-0.192	-0.192	**S19**	0.283	**0.325**
C6	-0.198	-0.200	**O20**	-0.635	-0.626
S7	2.335	**2.332**	**H21**	0.293	0.292
O8	-0.969	-0.965	**H22**	0.288	0.288
O9	-0.969	-0.973	**H23**	0.290	0.289
N10	-0.749	**-0.774**	**H24**	0.293	0.292
N11	-0.386	**-0.418**	**H25**	0.305	0.308
N12	0.529	0.529	**H26**	0.305	0.308
O13	-0.403	-0.404	**H27**	0.448	0.457
O14	-0.403	-0.405	**H28**	0.485	0.488

The f^+, f^-, f^0, and Δf values obtained from the Fukui function analysis of the isomers of compound **7** are presented in Table 4. The results indicate that, in both isomers, the sulfur atom within the thiazolidin-4-one ring exhibits nucleophilic character and is therefore susceptible to oxidation; however, this nucleophilicity and oxidation propensity are more pronounced in the *E* isomer. The nitrogen atom attached to the thiazolidin-4-one ring appears similarly nucleophilic and readily oxidizable in both isomers. Notably, the sulfonyl-bound nitrogen in the *Z* isomer and the CH_2 carbon in the thiazolidin-4-one ring of the *E* isomer emerge as the most prominent sites in terms of nucleophilicity and oxidation susceptibility. In both isomers, the nitro group is the primary region associated with reduction tendency and electrophilic character. With respect to potential radical reactions, the sulfur atom in the thiazolidin-4-one ring of the *E* isomer is identified as the dominant reactive center.

Table 4. Hirshfeld atomic charges and condensed Fukui functions for both isomers of compound **7**[a]

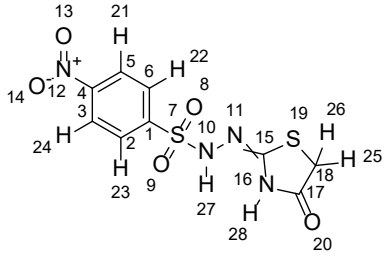

Atom Number	f^+		f^-		f^0		Δf	
	Z	***E***	***Z***	***E***	***Z***	***E***	***Z***	***E***
C1	0.054	0.054	0.000	0.000	0.027	0.026	0.054	0.054
C2	0.054	0.053	0.011	0.007	0.032	0.030	0.043	0.045
C3	0.090	0.094	0.009	0.006	0.049	0.050	0.081	0.088
C4	0.043	0.042	0.007	0.004	0.025	0.024	0.036	0.038
C5	0.094	0.090	0.009	0.006	0.051	0.048	0.085	0.084
C6	0.054	0.053	0.012	0.007	0.033	0.030	0.041	0.046
S7	0.017	0.016	0.023	0.014	0.020	0.015	-0.006	0.002
O8	0.017	0.017	0.047	0.022	0.031	0.019	-0.030	-0.004
O9	0.017	0.017	0.037	0.028	0.027	0.023	-0.020	-0.012
N10	0.009	0.013	**0.164**	0.057	0.087	0.035	**-0.155**	-0.044
N11	0.003	0.001	**0.179**	**0.173**	0.091	0.087	**-0.176**	**-0.172**
N12	**0.135**	**0.136**	0.002	0.001	0.068	0.068	**0.133**	**0.135**
O13	**0.200**	**0.201**	0.004	0.003	0.102	0.102	**0.196**	**0.198**
O14	**0.200**	**0.201**	0.004	0.003	0.102	0.102	**0.196**	**0.198**
C15	0.003	0.002	0.068	0.050	0.036	0.026	-0.066	-0.048
N16	0.002	0.003	0.081	0.055	0.041	0.029	-0.078	-0.053
C17	0.001	0.001	0.027	0.022	0.014	0.011	-0.026	-0.021
C18	0.003	0.002	0.082	**0.128**	0.042	0.065	-0.079	**-0.126**
S19	0.003	0.004	**0.177**	**0.363**	0.090	**0.184**	**-0.174**	**-0.360**
O20	0.002	0.002	0.058	0.050	0.030	0.026	-0.056	-0.049

[a]Hirshfeld atomic charges were calculated with hydrogen charges summed into the corresponding heavy atoms.

Proposed synthesis of compound 7

A synthetic route is proposed for he preparation of hybrid molecules formed by the combination of sulfonohydrazide and 1,3-thiazolidin-4-one moieties, starting from 4-nitrobenzenesulfonyl chloride (Scheme 1.). The proposed synthetic route involves a three-step sequence leading to the formation of the desired heterocyclic scaffold. In the first step, 4-nitrobenzenesulfonyl chloride was reacted with hydrazine hydrate to afford the corresponding 4-nitrobenzenesulfonohydrazide intermediate (**I**). This transformation is based on previously reported procedures and represents a convenient method for the preparation of sulfonohydrazide derivatives (Aslan, Özcan, & Karacan, 2012; Şenkardeş et al., 2021). In the second step, acylation of the sulfonohydrazide intermediate (**I**) with chloroacetyl chloride was proposed to yield the corresponding 2-chloro-*N*'-(4-nitrobenzene-1-sulfonyl)acetohydrazide derivative (**II**) (Brzozowski, Sławiński, Vullo, & Supuran, 2012). In the final step, the target compound, 4-nitro-*N*'-(4-oxo-1,3-thiazolidin-2-ylidene)benzene-1-sulfonohydrazide (**7**), was proposed to be synthesized through cyclization of compound **II** with ammonium thiocyanate. This reaction step is expected to result in the formation of the 1,3-thiazolidin-4-one ring system via intramolecular cyclization, as described in the literature (Kulabaş et al., 2017). Overall, the proposed synthetic route provides a straightforward approach for the preparation of the target compound from readily available starting materials. The suggested methodology is based on previously reported procedures and represents a feasible strategy for the synthesis of the designed derivative.

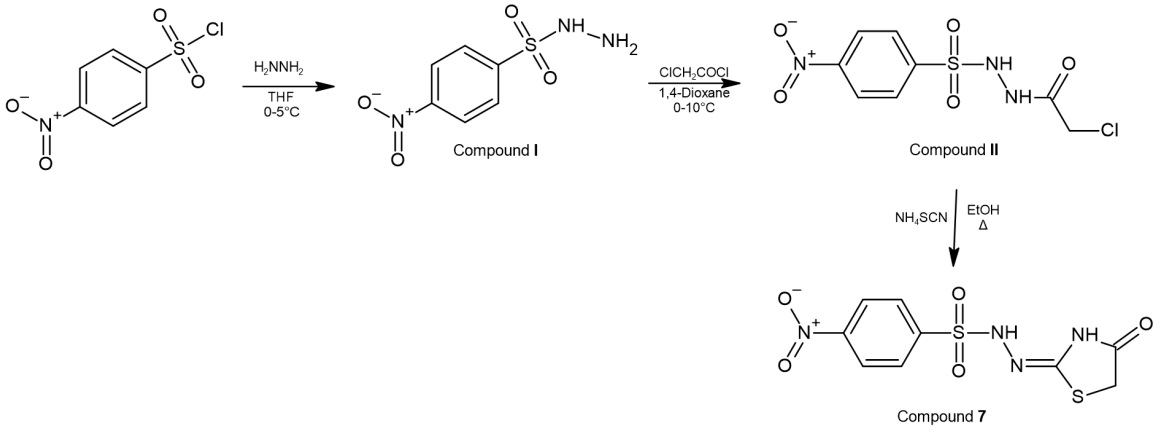

Scheme 1. The proposed synthetic scheme for the synthesis of the target compound **7**

***In silico* ADME and metabolism prediction**

SwissADME analysis revealed that the majority of the designed compounds exhibited favorable physicochemical and pharmacokinetic profiles, indicating potentially favorable oral pharmacokinetic properties. Most derivatives exhibited appropriate molecular weight ranges, balanced lipophilicity, and acceptable polarity values, indicating overall compliance with drug-likeness criteria. The predicted pharmacokinetic parameters demonstrated that most compounds have high gastrointestinal absorption, suggesting good oral bioavailability. In contrast, compounds **7** and **14** showed lower absorption profiles, which can be attributed to their increased polarity. Notably, none of the evaluated compounds violated Lipinski's rule of five, indicating generally favorable drug-like properties across the series. All compounds were predicted not to cross the blood–brain barrier, suggesting a reduced likelihood of central nervous system-related adverse effects. Cytochrome P450 inhibition analysis indicated that several derivatives may inhibit CYP1A2, while compound **12** additionally showed pre-

dicted inhibition of CYP2C19, suggesting a potential risk for metabolic drug–drug interactions in these molecules.

Among the evaluated derivatives, compound **7** exhibited a distinctive ADME profile characterized by exceptionally low lipophilicity (LogP = 0.06) and high polarity (TPSA = 167.13 Å²). Although these properties resulted in lower predicted gastrointestinal absorption, the increased polarity is expected to improve aqueous solubility and reduce nonspecific hydrophobic interactions. Importantly, compound **7** showed no predicted cytochrome P450 inhibition and no Lipinski's rule violations, suggesting a favorable predicted drug-likeness and metabolic interaction profile. The elevated polarity of this compound may contribute to its capacity to establish hydrogen bonding interactions within the enzyme binding site, which is particularly advantageous for RNA-dependent RNA polymerase inhibitors. Compared with remdesivir, compound **7** exhibited a markedly lower molecular weight (316.31 vs. 602.58 g/mol), lower lipophilicity (LogP 0.06 vs. 0.79), and a substantially smaller topological polar surface area (167.13 vs. 213.36 Å²). Although both compounds were predicted to have low gastrointestinal absorption and were not predicted to cross the blood–brain barrier, only compound **7** fully complied with Lipinski's Rule of Five, whereas remdesivir showed two violations, mainly due to its high molecular weight and polar surface area. Collectively, these findings suggest that compound **7** possesses a more favorable drug-likeness profile than remdesivir while maintaining a favorable predicted metabolic profile, highlighting its potential as a promising scaffold for further structural optimization and lead development.

Table 5. SwissADME-predicted physicochemical and pharmacokinetic properties of compounds **1**-**14** and remdesivir

Compound	MW (g/mol)	LogP	TPSA (Å²)	HBD/HBA	GI Abs.	BBB	RO5[a] Violations	CYP Inh.
1	271.32	0.64	121.31	2/4	High	No	0	No
2	285.34	1.12	121.31	2/4	High	No	0	No
3	289.31	1.11	121.31	2/5	High	No	0	No
4	305.76	1.15	121.31	2/4	High	No	0	CYP1A2
5	350.21	1.26	121.31	2/4	High	No	0	CYP1A2
6	301.34	0.67	130.54	2/5	High	No	0	No
7	316.31	0.06	167.13	2/6	Low	No	0	No
8	285.34	1.01	112.52	1/4	High	No	0	No
9	299.37	1.29	112.52	1/4	High	No	0	CYP1A2
10	303.33	1.33	112.52	1/5	High	No	0	No
11	319.79	1.53	112.52	1/4	High	No	0	CYP1A2
12	364.24	1.64	112.52	1/4	High	No	0	CYP1A2 CYP2C19
13	315.37	0.97	121.75	1/5	High	No	0	No
14	330.34	0.39	158.34	1/6	Low	No	0	CYP1A2
Remdesivir	602.58	0.79	213.36	4/12	Low	No	2	No[b]

[a] Lipinski's Rule of 5: MW ≤ 500 g/mol; LogP ≤ 5; HBA ≤ 10; HBD ≤ 5. MW, molecular weight; LogP, logarithm of the octanol/water partition coefficient; TPSA, topological polar surface area; HBD/HBA, hydrogen bond donor/hydrogen bond acceptor; GI Abs., gastrointestinal absorption; BBB, blood–brain barrier permeability; CYP Inh., cytochrome P450 inhibition.

[b] To date, no clinically significant enzyme inhibition of remdesivir has been reported.

The SwissADME bioavailability radar indicated that the majority of the designed compounds lie within the optimal physicochemical domain associated with good oral bioavailability (Figure 11.). The radar plot demonstrated balanced lipophilicity, molecular size, and polarity, suggesting favorable passive membrane diffusion. The limited deviations observed for solubility and saturation parameters indicate potential optimization points but do not significantly compromise the overall drug-likeness. These results support the rational design strategy and confirm that the target compounds exhibit promising pharmacokinetic characteristics.

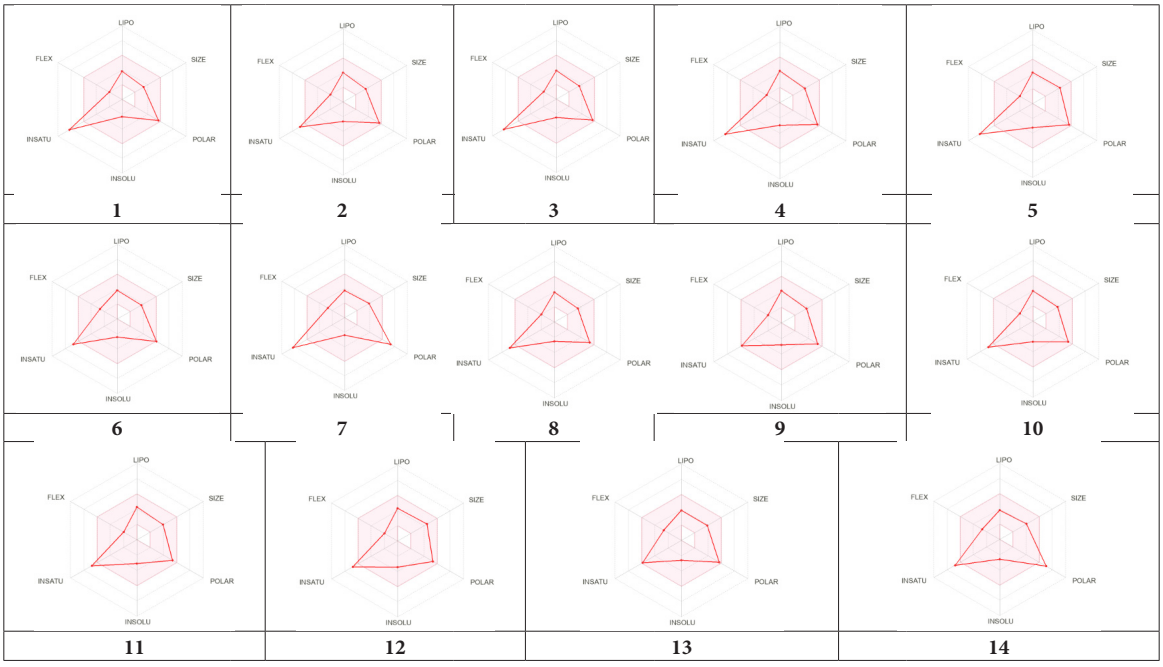

Figure 11. Bioavailability radar of the designed compounds **1**-**14**

BioTransformer 3.0 is an open-access computational platform designed to predict the biotransformation pathways and metabolic fate of small molecules (Wishart et al., 2022). The system combines machine-learning-based approaches with rule-based knowledge systems to model the transformation of xenobiotics -including drugs, pesticides, and dietary compounds- across human tissues, gut microbiota, and environmental matrices such as soil and water. Previous studies have demonstrated that BioTransformer provides highly accurate and comprehensive outputs, particularly in metabolite prediction and biotransformation pathway elucidation (Djoumbou Feunang et al., 2019). Nevertheless, outputs generated by BioTransformer 3.0 should not be interpreted as a complete representation of the full complexity of biological systems, but rather as predictive models that inform experimental design and support hypothesis generation. Analysis of compound **7**, which was identified through the *in silico* studies as having the highest predicted inhibitory potential against SARS-CoV-2 RdRp, revealed that its Phase I metabolism is predominantly governed by oxidative biotransformation pathways. Among the predicted metabolites, M1 is proposed to arise from a hydroxylation reaction at the 5-position of the 1,3-thiazolidin-4-one ring, most likely mediated by CYP1A2. Subsequent oxidative transformations involving the sulfur atom of the 1,3-thiazolidin-4-one moiety are predicted to yield metabolites M2 and M3 (Figure 12.), catalyzed by CYP3A4 and CYP2C9, respectively. In addition to Phase I metabolism, database predictions indicate

that compound **7** may undergo Phase II conjugation via its sulfonohydrazino group, leading to the formation of the glucuronidated metabolite M4. Following the identification of these metabolites and their associated enzymatic pathways, the absence of significant inhibitory activity of compound **7** toward cytochrome P450 enzymes suggests that it may be less likely to interfere with its own metabolic processing. However, it should be noted that alterations in enzyme activity -such as inhibition or induction- may significantly influence the compound's pharmacokinetic profile and duration of action.

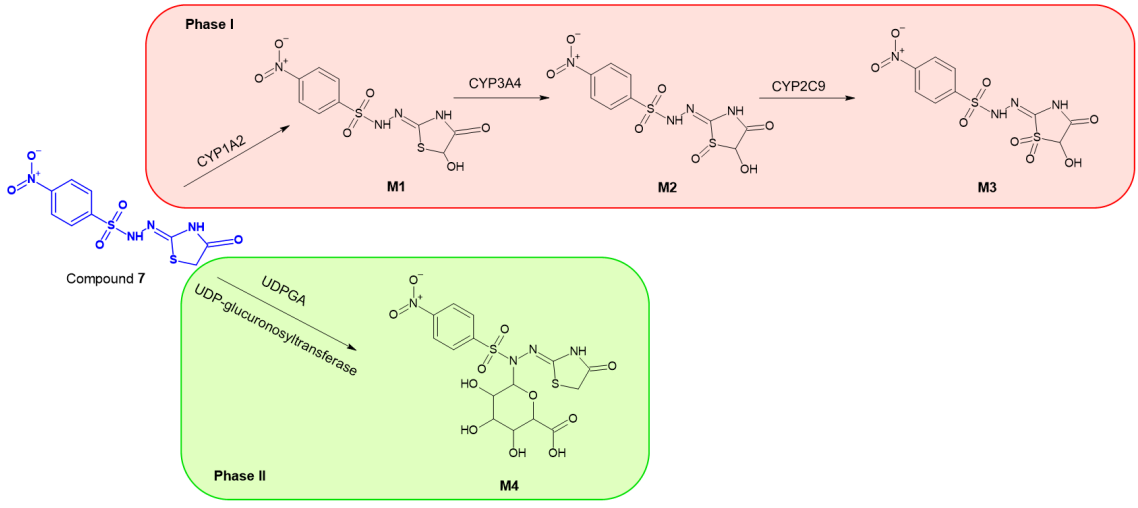

Figure 12. Predicted metabolic pathway of compound **7**

In conclusion, these *in silico* data provide important insights into the metabolic stability of compound **7**, the potential formation of active or toxic metabolites, and possible drug interactions. However, for these insights to become meaningful from a pharmacokinetic and toxicological perspective, they need to be supported by *in vitro* and *in vivo* studies, particularly regarding metabolite profile, enzyme kinetics, and glucuronidation rates.

CONCLUSION

The integrated computational analyses identified compound **7** as the most promising candidate within the designed series. Redocking of remdesivir monophosphate into the experimentally defined 7BV2 binding region reproduced the reference orientation with a heavy-atom RMSD of 1.097 Å, supporting the validity of the adopted docking protocol. Among the designed compounds, the *Z* isomer of compound **7** showed the most favorable docking profile (-9.27 kcal mol^{-1}; estimated K_i = 0.16 μM). Molecular dynamics simulations further highlighted differences between the two configurations: the *Z* isomer maintained a stable ligand RMSD of approximately 1.1-1.5 Å and persistent interactions with Gly590, Thr591, Lys593, and Phe594, whereas the *E* isomer underwent conformational reorientation before reaching a new stable state. Consistently, MM/GBSA analysis indicated more favorable average binding energetics for the *Z* isomer (-33.19 ± 2.97 $kcal.mol^{-1}$) than for the *E* isomer (-24.29 ± 2.96 $kcal.mol^{-1}$). DFT and condensed Fukui analyses revealed isomer-dependent electronic and local reactivity patterns, while ADME and metabolism predictions indicated favorable predicted drug-likeness and metabolic characteristics for compound **7** despite its high polarity and low predicted gastrointestinal absorption. Overall, these results prioritize compound **7**, particularly its *Z* isomer, as a scaffold for further optimization. However, the docking-derived affinity estimates and other computational findings remain predictive and require validation

by biochemical RdRp assays, cell-based antiviral studies, and experimental pharmacokinetic and toxicity evaluations.

ACKNOWLEDGMENTS

The numerical calculations reported in this paper were partially performed using TRUBA resources provided by the Turkish Academic Network and Information Center (ULAKBİM), High Performance and Grid Computing Center, Scientific and Technological Research Council of Türkiye (TÜBİTAK).

AUTHOR CONTRIBUTION STATEMENT

Conceptualization: N.K., S.Ş., S.Ç., E.A.; Methodology: N.K., S.Ş., S.Ç., E.A.; Molecular Docking Studies: S.Ç., E.A., N.K.; Molecular Dynamics Simulations: E.A., N.K.; Density Functional Theory (DFT) Calculations: E.A., N.K.; ADME and Metabolic Predictions: N.K., S.Ş.; Data Analysis and Interpretation: N.K., S.Ş., S.Ç., E.A.; Visualization: N.K., S.Ş., S.Ç., E.A.; Writing – Original Draft: N.K., S.Ş., S.Ç., E.A.; Writing – Review & Editing: N.K., S.Ş., S.Ç., E.A.; Supervision: N.K. All authors have read and approved the final manuscript.

CONFLICT OF INTEREST

The authors declare that there is no conflict of interest.

REFERENCES

Aslan, H. G., Özcan, S., & Karacan, N. (2012). The antibacterial activity of some sulfonamides and sulfonyl hydrazones, and 2D-QSAR study of a series of sulfonyl hydrazones. *Spectrochimica Acta Part A: Molecular and Biomolecular Spectroscopy, 98*, 329-336. doi:10.1016/j.saa.2012.08.043

BIOVIA. (2025). *Discovery Studio Visualizer, version 2026 [Computer software]*. Dassault Systèmes, San Diego, CA.

Bouysset, C. (2026). ProLIF, version 2.2.1 [Computer software]. Zenodo. doi:10.5281/zenodo.4386984

Bouysset, C., & Fiorucci, S. (2021). ProLIF: A library to encode molecular interactions as fingerprints. *Journal of Cheminformatics, 13*, 72. doi:10.1186/s13321-021-00548-6

Brzozowski, Z., Sławiński, J., Vullo, D., & Supuran, C. T. (2012). Carbonic anhydrase inhibitors. Regioselective synthesis of novel series 1-substituted 1,4-dihydro-4-oxo-3-pyridinesulfonamides and their inhibition of the human cytosolic isozymes I and II and transmembrane cancer-associated isozymes IX and XII. *European Journal of Medicinal Chemistry, 56*, 282-291. doi:10.1016/j.ejmech.2012.08.006

Case, D. A., Aktulga, H. M., Belfon, K., Cerutti, D. S., Cisneros, G. A., Cruzeiro, V. W. D.,…Merz, K. M. (2023). AmberTools. *Journal of Chemical Information and Modeling, 63*(20), 6183–6191. doi:10.1021/acs.jcim.3c01153

Case, D. A., Cerutti, D. S., Cruzeiro, V. W. D., Darden, T. A., Duke, R. E., Ghazimirsaeed, M.,…Merz, K. M. (2025). Recent developments in Amber biomolecular simulations. *Journal of Chemical Information and Modeling, 65*(15), 7835–7843. doi:10.1021/acs.jcim.5c01063

Cihan-Üstündağ, G., Gürsoy, E., Naesens, L., Ulusoy-Güzeldemirci, N., & Çapan, G. (2016). Synthesis and antiviral properties of novel indole-based thiosemicarbazides and 4-thiazolidinones. *Bioorganic & Medicinal Chemistry, 24*, 240-246. doi:10.1016/j.bmc.2015.12.008

Daina, A., Michielin, O., & Zoete, V. (2017). SwissADME: A free web tool to evaluate pharmacokinetics, drug-likeness and medicinal chemistry friendliness of small molecules. *Scientific Reports, 7*, 42717. doi:10.1038/srep42717

Dennington, R., Keith, T. A., & Millam, J. M. (2016). GaussView, version 6 [Computer software]. Semichem Inc., Shawnee Mission, KS.

Djoumbou Feunang, Y., Fiamoncini, J., de la Fuente, A. G., Manach, C., Greiner, R., & Wishart, D. S. (2019). BioTransformer: A comprehensive computational tool for small molecule metabolism prediction and metabolite identification. *Journal of Cheminformatics, 11*, 2. doi:10.1186/s13321-018-0324-5

Eberhardt, J., Santos-Martins, D., Tillack, A. F., & Forli, S. (2021). AutoDock Vina 1.2.0: New docking methods, expanded force field, and Python bindings. *Journal of Chemical Information and Modeling, 61*, 3891-3898. doi:10.1021/acs.jcim.1c00203

Elghoneimy, L. K., Ismail, M. I., Boeckler, F. M., Azzazy, H. M. E., & Ibrahim, T. M. (2021). Facilitating SARS-CoV-2 RNA-dependent RNA polymerase (RdRp) drug discovery by the aid of HCV NS5B palm subdomain binders: In silico approaches and benchmarking. *Computers in Biology and Medicine, 134*, 104468. doi:10.1016/j.compbiomed.2021.104468

El-Hddad, S. S. A., Sobhy, M. H., El-morsy, A., Shoman, N. A., & El-Adl, K. (2024). Quinazolines and thiazolidine-2,4-diones as SARS-CoV-2 inhibitors: Repurposing, in silico molecular docking and dynamics simulation. *RSC Advances, 14*, 13237-13250. doi:10.1039/D4RA02029D

Frisch, M. J., Trucks, G. W., Schlegel, H. B., Scuseria, G. E., Robb, M. A., Cheeseman, J. R.,...Fox, D. J. (2016). Gaussian 16, revision C.01 [Computer software]. Gaussian Inc., Wallingford, CT.

Gajjar, N. D., Dhameliya, T. M., & Shah, G. B. (2021). In search of RdRp and Mpro inhibitors against SARS-CoV-2: Molecular docking, molecular dynamic simulations and ADMET analysis. *Journal of Molecular Structure, 1239*, 130488. doi:10.1016/j.molstruc.2021.130488

Götz, A. W., Williamson, M. J., Xu, D., Poole, D., Le Grand, S., & Walker, R. C. (2012). Routine microsecond molecular dynamics simulations with AMBER on GPUs. 1. Generalized Born. *Journal of Chemical Theory and Computation, 8*(5), 1542–1555. doi:10.1021/ct200909j

Kline, T., Barry, K. C., Jackson, S. R., Felise, H. B., Nguyen, H. V., & Miller, S. I. (2009). Tethered thiazolidinone dimers as inhibitors of the bacterial type III secretion system. *Bioorganic & Medicinal Chemistry Letters, 19*, 1340-1343. doi:10.1016/j.bmcl.2009.01.047

Kulabaş, N., Bingöl Özakpınar, Ö., Özsavcı, D., Leyssen, P., Neyts, J., & Küçükgüzel, İ. (2017). Synthesis, characterization and biological evaluation of thioureas, acylthioureas and 4-thiazolidinones as anticancer and antiviral agents. *Marmara Pharmaceutical Journal*, *21*(2), 371-384. doi:10.12991/marupj.300913

Kulabaş, N., Lee, J. C., Bingöl Özakpınar, Ö., & Küçükgüzel, İ. (2024). Synthesis and anti-HCV activity of novel 5-arylmethylene-1,3-thiazolidin-4-one derivatives via suppression of NS5B polymerase and COX-2. *Journal of Molecular Structure, 1311*, 138407. doi:10.1016/j.molstruc.2024.138407

Mammeri, S., Kerkour, R., Chafai, N., Harkat, H., & Chafaa, S. (2025). Synthesis, characterization, DFT analysis, pharmacokinetics, and inhibition of Mpro and RdRp of SARS-CoV-2 by two di-

hydropyrimidines derivatives. *Journal of Molecular Structure, 1324*, 140797. doi:10.1016/j.molstruc.2024.140797

Mehyar, N., Samman, N., Al Gheribi, S., Mashhour, A., Chan, P., Al-Kaysi, R. O.,...Islam, I. (2025). First-in-class inhibitors of Nsp15 endoribonuclease of SARS-CoV-2: Modeling, synthesis, and enzymatic assay of thiazolidinedione and rhodanine analogs. *Journal of Biological Chemistry, 301*, 110409. doi:10.1016/j.jbc.2025.110409

Morris, G. M., Huey, R., Lindstrom, W., Sanner, M. F., Belew, R. K., Goodsell, D. S., & Olson, A. J. (2009). AutoDock4 and AutoDockTools4: Automated docking with selective receptor flexibility. *Journal of Computational Chemistry, 30,* 2785-2791. doi:10.1002/jcc.21256

Salomon-Ferrer, R., Götz, A. W., Poole, D., Le Grand, S., & Walker, R. C. (2013). Routine microsecond molecular dynamics simulations with AMBER on GPUs. 2. Explicit solvent particle mesh Ewald. *Journal of Chemical Theory and Computation, 9*(9), 3878–3888. doi:10.1021/ct400314y

Şenkardeş, S., & Küçükgüzel, Ş. G. (2016). Recent progress on synthesis and anticancer activity of 4-thiazolidinone. *Mini-Reviews in Organic Chemistry, 13,* 377-388. doi:10.2174/1570193X13666160826154159

Şenkardeş, S., Kart, D., Bebek, B., Gündüz, M. G., & Küçükgüzel, Ş. G. (2023). Synthesis, antimicrobial properties and in silico studies of aryloxyacetic acid derivatives with hydrazone or thiazolidine-4-one scaffold. *Journal of Biomolecular Structure and Dynamics*, *41*, 7421-7432. doi:10.1080/07391102.2022.2121761

Şenkardeş, S., Kıymacı, M. E., Kale, K., Kozanoğlu, İ. M., Kaşkatepe, B., & Küçükgüzel, Ş. G. (2021). Synthesis, structural elucidation and biological activities of some novel sulfonyl hydrazones as antibacterial agents. *Journal of Research in Pharmacy*, *25*(2), 135-141. doi:10.29228/jrp.4

Thakkar, J., Vaghani, H., Kardani, H., & Patel, P. (2025). Synthetic approaches to heterocyclic scaffolds: 4-thiazolidinone derivatives as heterocyclic scaffolds: Synthesis and biological activity (a review). *Russian Journal of Organic Chemistry, 61*, 765-799. doi:10.1134/S1234567824604856

Trott, O., & Olson, A. J. (2010). AutoDock Vina: Improving the speed and accuracy of docking with a new scoring function, efficient optimization, and multithreading. *Journal of Computational Chemistry, 31*, 455-461. doi:10.1002/jcc.21334

Wang, Y., Anirudhan, V., Du, R., Cui, Q., & Rong, L. (2021). RNA-dependent RNA polymerase of SARS-CoV-2 as a therapeutic target. *Journal of Medical Virology, 93,* 300-310. doi:10.1002/jmv.26264

Wavefunction Inc. (2004). *Spartan'04 [Computer software]*. Wavefunction Inc., Irvine, CA.

Wishart, D. S., Tian, S., Allen, D., Oler, E., Peters, H., Lui, V. W.,...Metz, T. O. (2022). BioTransformer 3.0—a web server for accurately predicting metabolic transformation products. *Nucleic Acids Research*, *50*(W1), W115-W123. doi:10.1093/nar/gkac313

World Health Organization. (n.d.), *COVID-19 cases | WHO COVID-19 dashboard*, https://data.who.int/dashboards/covid19/cases, Accessed: June 16, 2026.

Yin, W., Mao, C., Luan, X., Shen, D. D., Shen, Q., Su, H.,…Xu, H. E. (2020). Structural basis for inhibition of the RNA-dependent RNA polymerase from SARS-CoV-2 by remdesivir. *Science (New York, N.Y.), 368*(6498), 1499–1504. doi:10.1126/science.abc1560